Nano Research 2018, 11(5): 2562–2572
https://doi.org/10.1007/s12274-017-1881-z
Research Article
ISSN 1998-0124
CN 11-5974/O4

One-pot synthesis of interconnected $Pt_{95}Co_5$ nanowires with enhanced electrocatalytic performance for methanol oxidation reaction

Qingqing Lu[1,2], Litai Sun[1,2], Xue Zhao[1,2], Jianshe Huang[1], Ce Han[1], and Xiurong Yang[1] (✉)

[1] *State Key Laboratory of Electroanalytical Chemistry, Changchun Institute of Applied Chemistry, Chinese Academy of Sciences, Changchun 130022, China*
[2] *University of Chinese Academy of Sciences, Beijing100049, China*

Received: 10 August 2017
Revised: 30 September 2017
Accepted: 11 October 2017

© Tsinghua University Press and Springer-Verlag GmbH Germany 2017

KEYWORDS
platinum, cobalt, nanowires, methanol oxidation, electrocatalyst

ABSTRACT

Shape- and composition-controlled synthesis of platinum-based nanocrystals (NCs) is critical for the development of electrocatalysts that have high activity toward the methanol oxidation reaction (MOR) in direct methanol fuel cells (DMFCs). We report one-pot surfactant-free synthesis of interconnected $Pt_{95}Co_5$ nanowires (NWs) via an oriented attachment process, which has distinct advantages over conventional template- and surfactant-assisted approaches. Enhanced electrochemical activities toward MOR were confirmed through comparison with pure Pt NWs and commercial Pt/C catalyst. $Pt_{95}Co_5$ NWs demonstrated the highest current density during the long-term stability test. These results reveal that the introduction of the 3d-transition metal Co can reduce the catalyst cost and contribute to the improvement of electrochemical performance. The integrated design of interconnected NW structure, bimetallic composition, and clean surfaces in the present system may open a new way to the development of excellent electrocatalysts in DMFCs.

1 Introduction

With growing global demand for clean and sustainable energy sources, proton exchange membrane fuel cells (PEMFCs) have received much research attention due to their high energy density, low pollutant emission, and facile operating temperature [1–3]. Direct methanol fuel cells (DMFCs)—which directly convert the chemical energy of methanol to electricity—are considered potential power suppliers for automobiles and portable electronics [4, 5]. Developing highly active electrocatalysts for the methanol oxidation reaction (MOR) is an ideal way to realize the commercialization of this technology [6, 7]. To date, platinum is the most effective monometallic catalyst in DMFCs but the Pt surface is prone to poisoning by strongly adsorbed intermediate species, hindering MOR activity and long-term stability [8–10]. The low natural abundance

Address correspondence to xryang@ciac.ac.cn

and high price of Pt also severely limit its utilization [11]. Thus, it is desirable to design Pt-based bimetallic electrocatalysts to simultaneously minimize Pt consumption and improve electrochemical performance [12–14].

Following this research interest, Pt-based nanocrystals (NCs) including PtAu [15], PtRu [16], PtPd [17], PtCu [18], PtCo [19], and others [20] were studied. The most cost-effective choice is to combine Pt with a cheap 3d-transition metal such as Fe, Co, Ni, or Cu [21–24]. It has been reported that the introduction of 3d-transition metals in Pt-based NCs can weaken the adsorption of oxygenated species and increase the number of active sites [25–27]. Another way to increase Pt utilization is by controlling the shape of Pt-based NCs [28]. Zhang et al. demonstrated the synthesis of PtCu nanoframes with higher activity toward MOR than previously reported PtCu tetragonal superstructures and dendritic PtCu nanoparticles [29, 30]. Recent experiments indicated that one-dimensional (1D) Pt-based nanostructures such as nanowires (NWs), nanorods (NRs), and nanotubes (NTs) are less vulnerable to dissolution, aggregation, and Ostwald ripening than conventional nanoparticles [9]. They can also eliminate the corrosion of carbon supports due to their inherent self-supporting feature [31, 32]. The reported synthetic approaches for 1D nanostructures mainly include template-directed synthesis [33], direct decomposition of organometallic precursors [34], modified phase-transfer [35], and surfactant-mediated self-assembly [36]. Typically, PtRu NTs and PtRu/Cu NWs prepared by the galvanic replacement of Cu NWs show enhanced specific activities toward MOR relative to PtRu/C [37]. Chen et al. synthesized trimetallic PtPdCu NWs with tunable composition with the assistance of surfactant Triton X-114 [38]. Despite these successful demonstrations, the reported routes usually involved complicated multistep procedures and difficult conditions for removing capping agents, which are disadvantageous for large-scale synthesis [33, 36–38]. Development of a one-pot and surfactant-free route for the synthesis of Pt-based NWs in high yield is hence demanding.

To address the aforementioned issues, we present a one-pot solvothermal strategy for preparing bimetallic $Pt_{95}Co_5$ NWs. The oriented attachment mechanism was proposed to better understand the formation process. The integrated design of the 1D NW structure, bimetallic composition, and clean particle surfaces enhanced $Pt_{95}Co_5$ NWs activity and durability toward MOR relative to pure Pt NWs and commercial Pt/C catalyst. Owing to the straightforward synthesis and superior electrocatalytic properties, as-prepared $Pt_{95}Co_5$ NWs hold great potential for application in DMFCs.

2 Experimental

2.1 Materials

Hexachloroplatinic(IV) acid hexahydrate ($H_2PtCl_6{\cdot}6H_2O$), cobalt(II) chloride hexahydrate ($CoCl_2{\cdot}6H_2O$), potassium hydroxide (KOH), ethylene glycol, and N,N-dimethylformamide (DMF) were purchased from Beijing Chemical Reagent Company. Commercial Pt/C (20 wt.%) was obtained from Alfa Aesar. Nafion solution (5 wt.%) was obtained from Sigma Aldrich. All chemical reagents were used without further purification.

2.2 Synthesis of bimetallic PtCo NWs

KOH (500 mg), ethylene glycol (4 mL), and DMF (6 mL) were mixed in a small beaker (25 mL); then 200 μL of $H_2PtCl_6{\cdot}6H_2O$ (0.1 M) and 200 μL of $CoCl_2{\cdot}6H_2O$ (0.1 M) were added, followed by ultra-sonication treatment for 30 min. Subsequently, the homogeneous mixture was transferred to a 25 mL Teflon-lined stainless steel autoclave. The autoclave was maintained at 170 ˚C for 8 h and cooled naturally to room temperature. The resulting products were collected by centrifugation and washed three times with ethanol. To compare, Pt NWs were synthesized under identical conditions except for the addition of Co precursor [39].

2.3 Characterization

Transmission electron microscopy (TEM), high resolution TEM (HRTEM), high-angle annular dark-field scanning TEM (HAADF-STEM), and selected area electron diffraction (SAED) images were obtained using a JEM-2100F high-resolution transmission electron microscope operating at 200 kV. Scanning electron microscopy (SEM) and energy-dispersive X-ray (EDX)

spectroscopy were performed on an FEI XL30 ESEM FEG field-emission scanning electron microscope operating at 25 kV. Powder X-ray diffraction (XRD) patterns were recorded with a Bruker D8 ADVANCE diffractometer using Cu-Kα (0.154 nm) radiation. X-ray photoelectron spectroscopy (XPS) measurements were carried out using an ESCALAB-MKII spectrometer with an Al-Kα X-ray light source, calibrated against the C 1s level (284.8 eV). The exact composition of $Pt_{95}Co_5$ NWs was determined using inductively coupled plasma-optical emission spectrometry (ICP-OES, X Series 2, Thermo Scientific USA).

2.4 Electrochemical measurements

Electrochemical experiments were performed in conventional three-electrode cells using a CHI 832 electrochemical workstation. An Ag/AgCl (saturated KCl) electrode, a glassy carbon electrode (GCE, 3 mm diameter), and a Pt wire were used as the reference, working, and counter electrodes, respectively. To prepare the working electrode, the GCE was carefully polished with Al_2O_3 slurry. The PtCo NWs were diluted to 2 mg·mL^{-1} in aqueous solution and 3 μL of catalyst ink was dropped on the electrode. Based on the ICP-OES measurement, the calculated Pt loading amount was 83.7 μg·cm^{-2}. The working electrode was then covered with 3 μL of 0.05 wt.% Nafion aqueous solution and dried at room temperature. The Pt loading amounts of Pt NWs and Pt/C catalyst were kept as those of PtCo NWs to assess their electrochemical performances. Before cyclic voltammetry (CV) measurements, the catalyst surface was first cleaned by cycling between −0.2 and 1.2 V to obtain a stable curve in N_2-saturated 0.5 M H_2SO_4 solution. Methanol oxidation measurement was performed in a mixture of 0.5 M H_2SO_4 and 1.0 M CH_3OH cycled between 0 and 1.0 V with a scan rate of 50 mV·s^{-1}. Chronoamperometric (CA) curves were recorded for 3,600 s at 0.6 V.

3 Results and discussion

3.1 Structural properties

Bimetallic PtCo NWs were directly synthesized by a modified one-pot solvothermal method with $H_2PtCl_6{\cdot}6H_2O$ and $CoCl_2{\cdot}6H_2O$ as metal precursors in the presence of DMF, KOH, and ethylene glycol (see Experimental section). Based on the Pt/Co atomic ratio calculated from the EDX spectrum (Fig. S1 in the Electronic Supplementary Material (ESM)), we denote the as-prepared PtCo NWs as $Pt_{95}Co_5$ NWs. The atomic ratio of Pt/Co obtained by ICP-OES was 95.4:4.6, which is consistent with the EDX analysis. The conversion efficiency of Pt precursor to $Pt_{95}Co_5$ NWs was 83.9%, whereas the yield of Co was only 4.4%. The reason for the preferential reduction of Pt compared to Co is possibly due to the much higher reduction potential of Pt(IV) (+0.71 V vs. SHE) relative to that of Co(II) (−0.23 V vs. SHE) [21, 40]. The morphology and structure of as-synthesized $Pt_{95}Co_5$ NWs were examined by SEM and TEM. As illustrated in Fig. 1(a), interconnected $Pt_{95}Co_5$ NWs were dense and dozens of micrometers in length. TEM images (Figs. 1(b) and 1(c)) reveal that the NWs were arranged into parallel nanobundles with average diameter of 20.55 nm, which is in sharp contrast to the reported structure of sole NW [21, 27, 32]. A closer view from Fig. 1(d) shows that one bunch of NWs was composed of 5–8 ultrathin NWs. This ultrathin feature is beneficial for enhancing electrocatalytic activity owing to the increase in available active sites [20]. The SAED pattern (inset in Fig. 1(d)) gives a single set of concentric rings indexed to the (111), (200), (220), and (311) planes, suggesting polycrystalline nature of the $Pt_{95}Co_5$ NWs [41]. HRTEM images (Figs. 1(e) and 1(f)) show clear lattice fringes extending coherently across the NWs without obvious phase segregation, implying the insertion of Co atoms in the Pt lattice would not cause an undesired microscopic phase. The measured interplanar distance of 0.224 nm corresponds to the (111) facets of face-centered-cubic (fcc) PtCo NCs [14, 22, 23].

The porous structure cross-linked by NWs was verified via HAADF-STEM images at different magnifications (Figs. 2(a)–2(c)). These pores are favorable for the adsorption and diffusion of guest species involved in MOR, thereby facilitating the reaction [15, 42]. Figures 2(d)–2(f) display the homogeneous distribution of Pt and Co throughout the $Pt_{95}Co_5$ NWs, confirming the formation of uniform PtCo alloy. In the control experiment, we performed

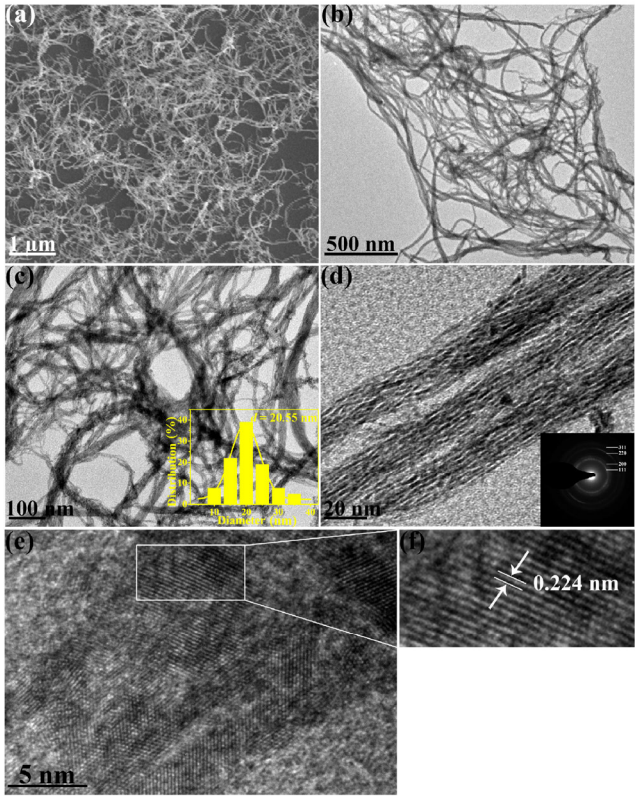

Figure 1 (a) SEM image, (b)–(d) TEM images, (e) HRTEM image, and (f) magnified HRTEM image of the rectangle area in (e) of $Pt_{95}Co_5$ NWs. The inset in (c) shows the size distribution histogram of $Pt_{95}Co_5$ nanobundles. The inset in (d) is the SAED pattern of $Pt_{95}Co_5$ NWs.

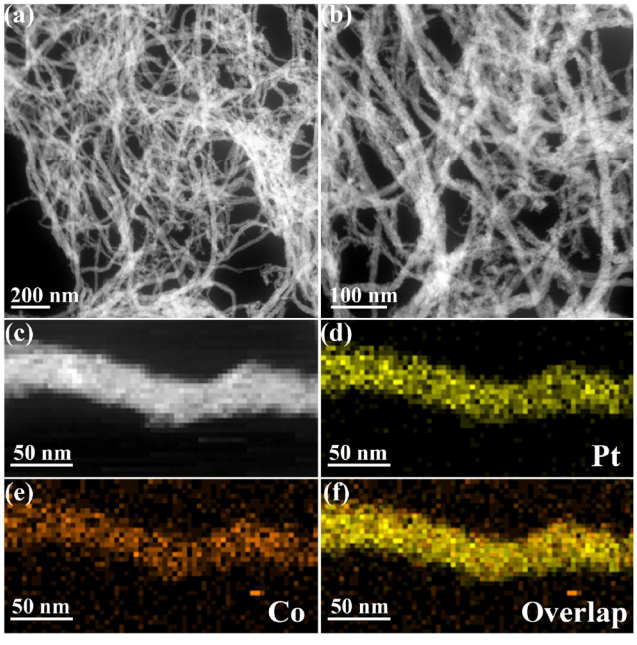

Figure 2 (a)–(c) HAADF-STEM images and (d)–(f) elemental mapping images of $Pt_{95}Co_5$ NWs.

various experiments to tune the Pt/Co ratio of the resulting PtCo NWs. Reducing the amounts of the two metallic precursors in half, the as-synthesized product still exhibited well-defined NW structure (Fig. S2(a) in the ESM). However, the Pt/Co composition remained constant (Fig. S2(b) in the ESM), thus excluding the possibility of insufficient reducing agent in the present system. Varying the feed ratio of Pt and Co precursors between 3:1 and 1:3, similar morphologies were observed (Fig. S3 in the ESM). The final atomic ratios between Pt and Co determined from EDX spectra were the same (Fig. S4 in the ESM), demonstrating that the initial Pt/Co ratio had little influence on the final composition of PtCo NWs. With further reduction in the amount of Pt precursor and increased amount of Co precursor, the aggregated NCs were dominant and the yield of NWs was low due to interruption of the nucleation step of Pt precursor (Figs. S5(a) and S5(b) in the ESM). Furthermore, if only Co precursor was added with other reaction parameters unchanged, the resulting products were mainly irregularly structured rather than NWs (Fig. S6 in the ESM). This fact highlights the role of Pt precursor in directing wire-like construction [43].

The crystal structure of $Pt_{95}Co_5$ NWs was further detected by powder XRD (Fig. 3(a)). The peaks at 40.1°, 46.2°, 67.6°, and 81.8° can be ascribed to the (111), (200), (220), and (311) planes, respectively, and no peaks corresponding to pure Pt and Co or their oxides were detected. These peaks were well correlated but shifted to slightly higher angles relative to standard Pt (JCPDS-04-0802), showing the merging of Co into the Pt lattice. This phenomenon was also observed in previous reports [22, 26]. The presence of only the PtCo fcc structure in both SAED and XRD patterns further reveals the formation of single-phase

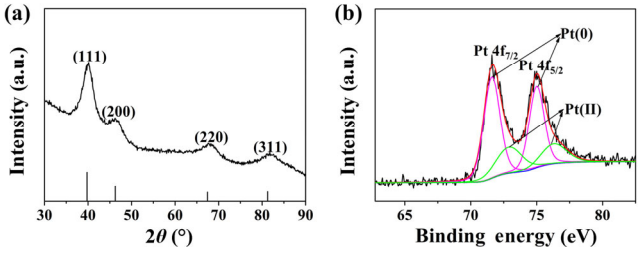

Figure 3 (a) XRD pattern and (b) deconvolution of Pt 4f XPS in $Pt_{95}Co_5$ NWs. The intensity and position of Pt at the bottom of (a) were taken from the JCPDS database (JCPDS No. 04-0802).

PtCo alloy [44], which is in agreement with the elemental mapping analysis. The most intense (111) peak was consistent with the dominant (111) facets determined by HRTEM. The composition and electronic structure of $Pt_{95}Co_5$ NWs were investigated by XPS. Figure 3(b) shows deconvolution of the Pt 4f spectrum of $Pt_{95}Co_5$ NWs. The Pt $4f_{7/2}$ peak at 71.6 eV and Pt $4f_{5/2}$ peak at 75.0 eV were assigned to metallic Pt while the peaks at 72.9 and 76.3 eV were attributed to PtO or $Pt(OH)_2$ [45]. Notably, the Pt $4f_{7/2}$ binding energy shifted to a slightly higher value relative to bulk Pt (71.2 eV) due to the incorporation of Co [46]. This change indicates the formation of PtCo alloy. In addition, downshift of the d-band center also favors the oxidation of intermediates during the MOR [22]. Furthermore, the high percentage of zero-valent Pt also contributed to the improvement of catalytic activity [39]. The ill-defined Co 2p spectrum confirms the existence of a low content of Co in $Pt_{95}Co_5$ NWs (Fig. S7 in the ESM) [47].

3.2 Formation mechanism

To investigate the process of forming bimetallic $Pt_{95}Co_5$ NWs, the morphologies of the $Pt_{95}Co_5$ NWs were tracked with time-dependent TEM experiments. As shown in Figs. S8(a) and S8(b) in the ESM, small nanoparticles, elongated nanorods, and some nanochains were formed in the first half hour. These adjacent nanoparticles underwent further ripening, fusion, and growth under solvothermal conditions [39, 48]. They preferred to coalesce and assemble in a wire-like structure. The NWs started to align side-by-side to reduce the total surface free energy (Fig. S8(c) in the ESM), and the strong cohesive interaction mainly originated from the adsorption of DMF [48]. As the reaction time increased (Fig. S8(d) in the ESM), the porous wire-like structure became clearer. After 5 h, well-defined $Pt_{95}Co_5$ NW assemblies were formed (Fig. S8(e) in the ESM). The interwoven $Pt_{95}Co_5$ NW bundles remained even when we extended the reaction time to 12 h (Fig. S8(f) in the ESM). Based on these results, we may deduce that the formation of PtCo NWs followed an oriented attachment mechanism rather than a seed-initiated oriented growth process [18, 39, 48, 49]. Similar to the well-established oleylamine-assisted synthesis of 1D nanomaterials [9, 50], the amine species released from the reaction of DMF and KOH guided the growth of PtCo nanoparticles and their subsequent self-assembly into NW bundles. Unlike previously reported syntheses of PtCo NWs that included various substrates, templates, organometallic precursors, and surfactants [27, 40, 51, 52], the present synthetic strategy is cost-effective and efficient.

3.3 Electrocatalytic performance

Encouraged by the intriguing morphology and bimetallic composition of the $Pt_{95}Co_5$ NWs, we evaluated the electrochemical performance toward MOR in acid medium. Pt NWs (Figs. S9(a) and S9(b) in the ESM) and commercial Pt/C catalyst were used as references. Figure 4(a) shows CV curves of $Pt_{95}Co_5$ NWs, Pt NWs, and commercial Pt/C in N_2-saturated 0.5 M H_2SO_4 solution at a sweep rate of 50 $mV \cdot s^{-1}$. By integrating the charges associated with the hydrogen desorption region after double-layer correction and assuming 210 $\mu C \cdot cm^{-2}$ for the monolayer adsorption of hydrogen on the Pt surface [22, 23], the electrochemically active surface areas (ECSAs) of $Pt_{95}Co_5$ NWs, Pt NWs, and Pt/C were estimated to be 23.1, 28.6, and 60.7 $m^2 \cdot g^{-1}$, respectively. The lower ECSA value of the NWs than that of Pt/C is likely due to the larger size of the nanobundle structure, while the larger ECSA of Pt/C may be due to the high surface area carbon support and smaller particle size. Figure 4(b) shows CV curves of $Pt_{95}Co_5$ NWs, Pt NWs, and commercial Pt/C toward MOR. All cases exhibited two well-defined peaks: The forward peak was associated with the oxidation of freshly-adsorbed methanol molecules whereas the backward peak was related to the removal of intermediate carbonaceous species. The current densities were normalized by the Pt mass to compare their mass activities. $Pt_{95}Co_5$ NWs exhibited the highest mass activity of 491.4 $mA \cdot mg_{Pt}^{-1}$, which was 1.7 and 2.2 times higher than Pt NWs (290.8 $mA \cdot mg_{Pt}^{-1}$) and Pt/C (228.3 $mA \cdot mg_{Pt}^{-1}$), respectively. Meanwhile, the specific activity of $Pt_{95}Co_5$ NWs was 2.13 $mA \cdot cm^{-2}$, which was almost 2.1- and 5.6-fold higher than those of Pt NWs (1.02 $mA \cdot cm^{-2}$) and Pt/C (0.38 $mA \cdot cm^{-2}$), respectively (Fig. S10 in the ESM). The improved performance is further highlighted by the histograms in Fig. 4(c). Although the ECSA of $Pt_{95}Co_5$ NWs was

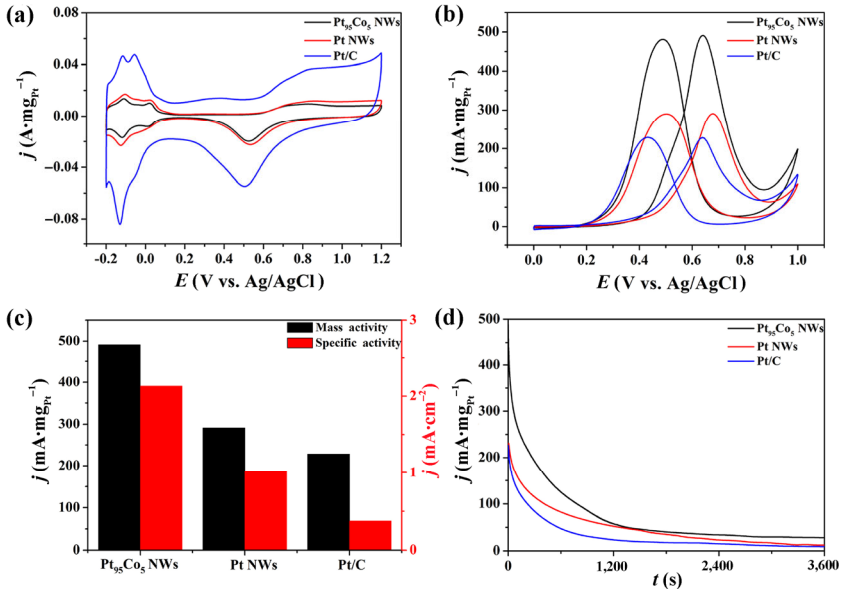

Figure 4 CV curves of $Pt_{95}Co_5$ NWs, Pt NWs, and Pt/C in (a) N_2-saturated 0.5 M H_2SO_4 solution and (b) 0.5 M H_2SO_4 + 1.0 M CH_3OH solution at a scan rate of 50 $mV \cdot s^{-1}$. (c) Specific activity and mass activity. (d) CA curves of $Pt_{95}Co_5$ NWs, Pt NWs, and Pt/C in 0.5 M H_2SO_4 + 1.0 M CH_3OH solution recorded at 0.6 V.

lower than that of Pt/C catalyst, it exhibited higher current density owing to its abundant active catalytic sites, which could adsorb methanol molecules at different sites and in different directions. Meanwhile, Pt in as-synthesized $Pt_{95}Co_5$ NWs was dispersed well and distributed, whereas Pt nanoparticles in Pt/C suffered from aggregation and detachment from carbon surfaces during electrochemical measurement. Pure Pt species are easily poisoned by intermediates adsorbed on electrode surfaces, but the synergistic effect between Pt and Co in $Pt_{95}Co_5$ NWs can contribute to C–H bond cleavage and the removal of poisonous species during the MOR. As summarized in Table S1 in the ESM, the observed activity of $Pt_{95}Co_5$ NWs toward MOR exceeded those of Pt-based nanomaterials previously reported in literature. Generally, the ratio of the forward peak current (I_f) to the backward peak current (I_b) I_f/I_b can be used to assess the catalyst poisoning tolerance to CO-like intermediates generated during methanol oxidation. $Pt_{95}Co_5$ NWs presented the highest I_f/I_b value of 1.02, indicating nearly complete oxidation of methanol to carbon dioxide on the electrode surface. This value was also higher than reported for hollow Pt-Pd nanospheres [17], nanoporous Pt-Co NWs [40], and Pd@Pt nanodendrites [53]. It agreed with the report that a small amount of Co can improve the tolerance to CO-like intermediates during the MOR [54].

Electrochemical durability is another vital factor for evaluating a practical catalyst. As shown in Fig. 4(d), all these catalysts exhibited sharp drops of current density in the initial stage followed by slower decay till eventually reaching stable states. The decay of current density was mainly caused by the accumulation and adsorption of carbonaceous species such as CO_{ads}, CHO_{ads}, and $COOH_{ads}$. These intermediates can occupy active sites and decrease the activity and durability of the catalyst. Nevertheless, $Pt_{95}Co_5$ NWs had a much higher current density than Pt NWs and Pt/C throughout the entire process, confirming their superior durability and good anti-poisoning capability. After the stability test, the catalysts were reactivated and evaluated for MOR. The ECSAs of the $Pt_{95}Co_5$ NWs, Pt NWs, and Pt/C reduced to 83.7%, 79.0%, and 48.1% of the initial values, respectively (Figs. 5(a), 5(c), and 5(e)). There was no obvious change in forward peak current density of $Pt_{95}Co_5$ NWs (Fig. 5(b)), while Pt NWs and Pt/C lost 3.8% and 48.2% of the original mass activity, respectively (Figs. 5(d) and 5(f)). The specific activity of $Pt_{95}Co_5$ NWs increased from 2.13 to 2.54 $mA \cdot cm^{-2}$ after electrochemical activation, indicating the effective removal of intermediates. The number of active

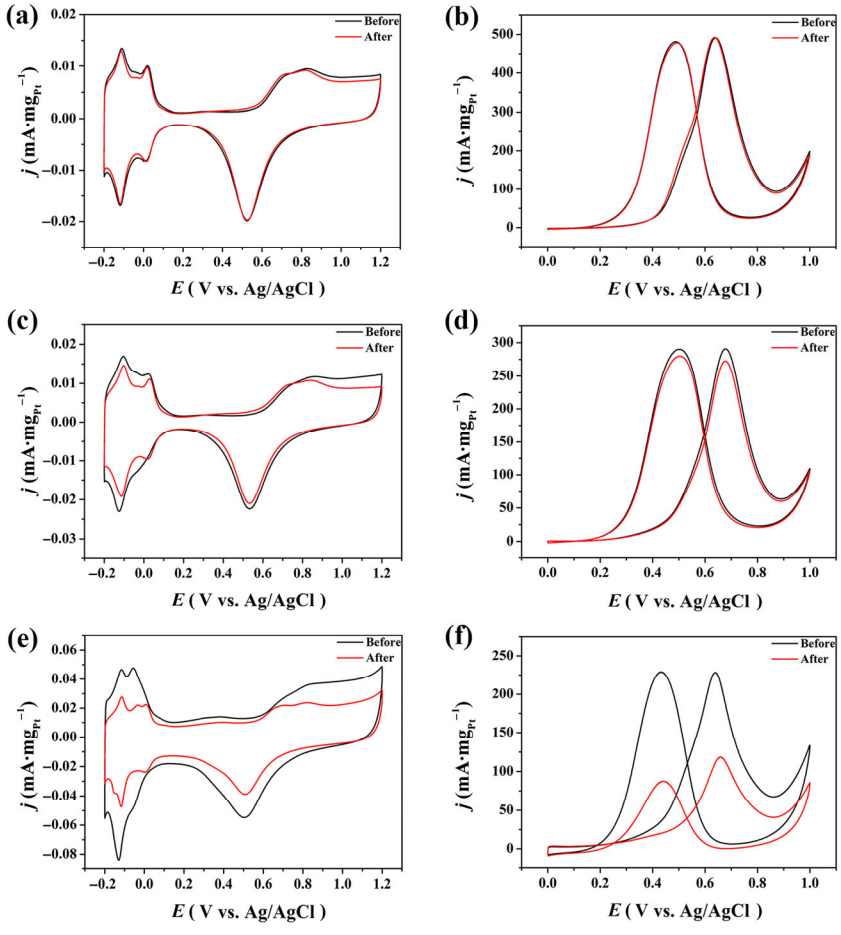

Figure 5 CV curves for (a) and (b): $Pt_{95}Co_5$ NWs, (c) and (d): Pt NWs, and (e) and (f): Pt/C before and after stability testing in N_2-saturated 0.5 M H_2SO_4 solution and 0.5 M H_2SO_4 + 1.0 M CH_3OH solution at a scan rate of 50 mV·s^{-1}, respectively.

catalytic sites was highly conserved owing to its three-dimensional (3D) network structure. This point was further confirmed in the TEM image of $Pt_{95}Co_5$ NWs after the durability test (Fig. S11 in the ESM). As expected, $Pt_{95}Co_5$ NWs retained their wire-like morphology, and no obvious aggregates were observed. This provides further verification of the improved durability of $Pt_{95}Co_5$ NWs.

Figures 6(a), 6(c), and 6(e) show CV curves of $Pt_{95}Co_5$ NWs, Pt NWs and Pt/C toward the MOR at different scan rates (50, 75, 100, 150, 200, and 250 mV·s^{-1}). The peak current density increased with increasing scan rate and the peak potential gradually shifted to higher potential. This trend reveals that the MOR on these electrodes was completely irreversible. The peak current densities were linearly proportional to the square of scan rate, indicating that MOR is a diffusion-controlled process [55]. The corresponding slopes for $Pt_{95}Co_5$ NWs, Pt NWs, and Pt/C were 13.3, 8.4 and 12.1, respectively (Figs. 6(b), 6(d), and 6(f)). The larger slope of $Pt_{95}Co_5$ NWs implies improved MOR kinetics on the bimetallic PtCo NWs relative to Pt NWs and Pt/C [56].

The aforementioned results clearly reveal the excellent activity and durability of $Pt_{95}Co_5$ NWs toward MOR, which are ascribed to the synergistic effect of the 1D NW structure and bimetallic PtCo composition. The interconnected NWs provide increased accessible active sites for the adsorption and diffusion of reaction species, leading to improved reaction kinetics during the MOR. Meanwhile they had better resistance to dissolution, coalescence, and migration than conventional nanoparticles, which should help with superior stability. Secondly, the presence of Co facilitated the removal of strongly bound intermediates on the sites neighboring Co, effectively improving their anti-poisoning ability [57]. Furthermore, alloying Pt with

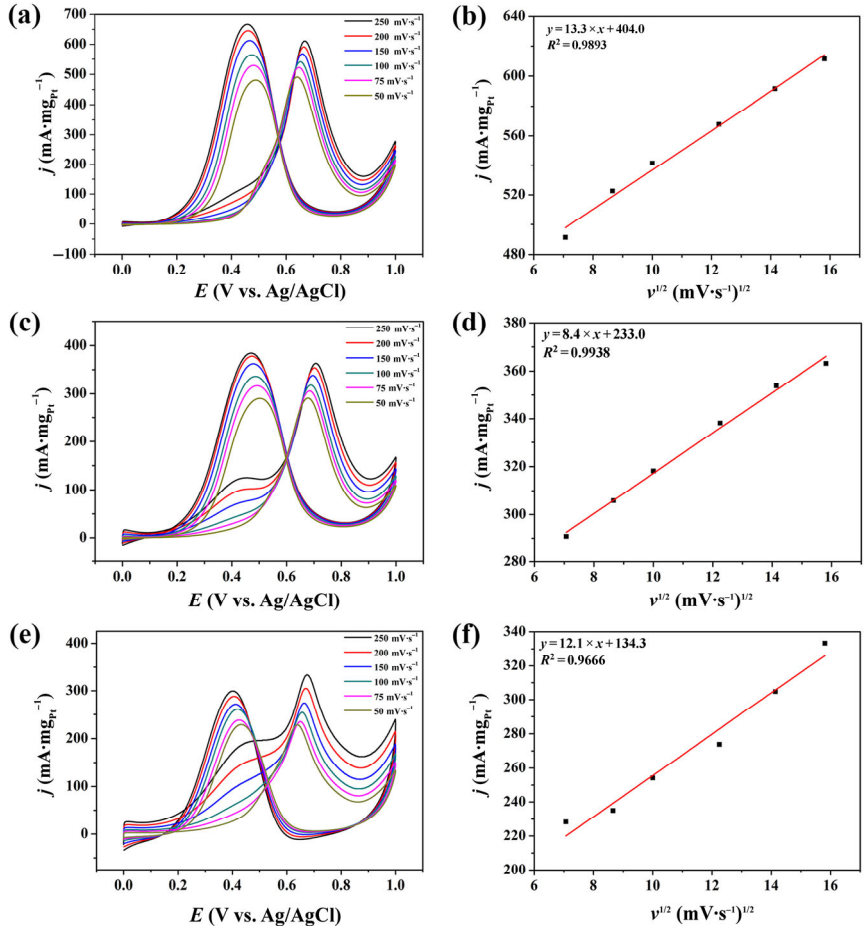

Figure 6 CV curves and the linear relationship between peak current density and the square root of scan rate for (a) and (b): $Pt_{95}Co_5$ NWs, (c) and (d): Pt NWs, and (e) and (f): Pt/C in 0.5 M H_2SO_4 + 1.0 M CH_3OH at different scan rates (scan rate: 50, 75, 100, 150, 200, and 250 $mV·s^{-1}$).

Co can lower the adsorption energies of adsorbates, and promote C-H bond cleavage at lower potential [22]. Besides, such surfactant-free synthesis is also advantageous for enhanced methanol oxidation activity due to the exposed clean surfaces.

4 Conclusions

Bimetallic $Pt_{95}Co_5$ NWs were successfully synthesized by a one-pot solvothermal method. No pre-made templates, organometallic precursors, or surfactants were used in the preparation process. Electrochemical measurements show that the $Pt_{95}Co_5$ NWs had superior activity and durability toward MOR relative to Pt NWs and Pt/C. These excellent properties can be attributed to the unique NW structure and bimetallic composition. The synthetic strategy we propose was confirmed to be effective for developing highly active electrocatalysts in DMFCs.

Acknowledgements

The authors gratefully acknowledge the financial support from the National Natural Science Foundation of China (Nos. 21435005 and 21627808), the Development Project of Science and Technology of Jilin Province (No. 20170101195JC), and Key Research Program of Frontier Sciences, Chinese Academy of Sciences (No. QYZDY-SSW-SLH019).

Electronic Supplementary Material: Supplementary material (EDX spectra and TEM images of PtCo NWs with different feed ratios and the performance comparison of as-prepared $Pt_{95}Co_5$ NWs with reported

other electrocatalysts) is available in the online version of this article at https://doi.org/10.1007/s12274-017-1881-z.

References

[1] Wang, Y.; Chen, K. S.; Mishler, J.; Cho, S. C.; Adroher, X. C. A review of polymer electrolyte membrane fuel cells: Technology, applications, and needs on fundamental research. *Appl. Energy* **2011**, *88*, 981–1007.

[2] Xu, W.; Wu, Z. C.; Tao, S. W. Recent progress in electrocatalysts with mesoporous structures for application in polymer electrolyte membrane fuel cells. *J. Mater. Chem. A* **2016**, *4*, 16272–16287.

[3] Peighambardoust, S. J.; Rowshanzamir, S.; Amjadi, M. Review of the proton exchange membranes for fuel cell applications. *Int. J. Hydrogen Energy* **2010**, *35*, 9349–9384.

[4] Zhao, X.; Yin, M.; Ma, L.; Liang, L.; Liu, C. P.; Liao, J. H.; Lu, T. H.; Xing, W. Recent advances in catalysts for direct methanol fuel cells. *Energy Environ. Sci.* **2011**, *4*, 2736–2753.

[5] Koenigsmann, C.; Wong, S. S. One-dimensional noble metal electrocatalysts: A promising structural paradigm for direct methanol fuel cells. *Energy Environ. Sci*. **2011**, *4*, 1161–1176.

[6] Chen, A. C.; Holt-Hindle, P. Platinum-based nanostructured materials: Synthesis, properties, and applications. *Chem. Rev.* **2010**, *110*, 3767–3804.

[7] Kakati, N.; Maiti, J.; Lee, S. H.; Viswanathan, B.; Yoon, Y. S. Anode catalysts for direct methanol fuel cells in acidic media: Do we have any alternative for Pt or Pt-Ru? *Chem. Rev.* **2014**, *114*, 12397–12429.

[8] Wang, L.; Yamauchi, Y. Block copolymer mediated synthesis of dendritic platinum nanoparticles. *J. Am. Chem. Soc.* **2009**, *131*, 9152–9153.

[9] Xia, B. Y.; Ng, W. T.; Wu, H. B.; Wang, X.; Lou, X. W. Self-supported interconnected Pt nanoassemblies as highly stable electrocatalysts for low-temperature fuel cells. *Angew. Chem., Int. Ed.* **2012**, *51*, 7213–7216.

[10] Sun, X. H.; Zhu, X.; Zhang, N.; Guo, J.; Guo, S. J.; Huang, X. Q. Controlling and self assembling of monodisperse platinum nanocubes as efficient methanol oxidation electrocatalysts. *Chem. Commun.* **2015**, *51*, 3529–3532.

[11] Liu, H. L.; Nosheen, F.; Wang, X. Noble metal alloy complex nanostructures: Controllable synthesis and their electrochemical property. *Chem. Soc. Rev.* **2015**, *44*, 3056–3078.

[12] Gilroy, K. D.; Ruditskiy, A.; Peng, H. C.; Qin, D.; Xia, Y. N. Bimetallic nanocrystals: Syntheses, properties, and applications. *Chem. Rev*. **2016**, *116*, 10414–10472.

[13] Wang, D. S.; Li, Y. D. Bimetallic nanocrystals: Liquid-phase synthesis and catalytic applications. *Adv. Mater.* **2011**, *23*, 1044–1060.

[14] Jiang, L.-Y.; Huang, X.-Y.; Wang, A.-J.; Li, X.-S.; Yuan, J. H.; Feng, J.-J. Facile solvothermal synthesis of $Pt_{76}Co_{24}$ nanomyriapods for efficient electrocatalysis. *J. Mater. Chem. A* **2017**, *5*, 10554–10560.

[15] Lu, Q. Q.; Wei, C. T.; Sun, L. T.; Alothman, Z. A.; Malgras, V.; Yamauchi, Y.; Wang, H. J.; Wang, L. Smart design of hollow AuPt nanospheres with a porous shell as superior electrocatalysts for ethylene glycol oxidation. *RSC Adv*. **2016**, *6*, 19632–19637.

[16] Lu, S. L.; Eid, K.; Ge, D. H.; Guo, J.; Wang, L.; Wang, H. J.; Gu, H. W. One-pot synthesis of PtRu nanodendrites as efficient catalysts for methanol oxidation reaction. *Nanoscale* **2017**, *9*, 1033–1039.

[17] Lu, Q. Q.; Wang, H. J.; Eid, K.; Alothman, Z. A.; Malgras, V.; Yamauchi, Y.; Wang, L. Synthesis of hollow platinum-palladium nanospheres with a dendritic shell as efficient electrocatalysts for methanol oxidation. *Chem.— Asian. J.* **2016**, *11*, 1939–1944.

[18] Zhu, C. Z.; Shi, Q. R.; Fu, S. F.; Song, J. H.; Xia, H. B.; Du, D.; Lin, Y. H. Efficient synthesis of MCu (M = Pd, Pt, and Au) aerogels with accelerated gelation kinetics and their high electrocatalytic activity. *Adv. Mater.* **2016**, *28*, 8779–8783.

[19] Wang, D.; Xin, H. L.; Hovden, R.; Wang, H.; Yu, Y.; Muller, D. A.; DiSalvo, F. J.; Abruña, H. D. Structurally ordered intermetallic platinum-cobalt core-shell nanoparticles with enhanced activity and stability as oxygen reduction electrocatalysts. *Nat. Mater.* **2013**, *12*, 81–87.

[20] Narayanamoorthy, B.; Ramanatha Datta, K. K.; Eswaramoorthy, M.; Balaji, S. Highly active and stable Pt_3Rh nanoclusters as supportless electrocatalyst for methanol oxidation in direct methanol fuel cells. *ACS Catal.* **2014**, *4*, 3621–3629.

[21] Eid, K.; Ahmad, Y. H.; AlQaradawi, S. Y.; Allam, N. K. Rational design of porous binary Pt-based nanodendrites as efficient catalysts for direct glucose fuel cells over a wide pH range. *Catal. Sci. Technol.* **2017**, *7*, 2819–2827.

[22] Xia, B. Y.; Wu, H. B.; Li, N.; Yan, Y.; Lou, X. W.; Wang, X. One-pot synthesis of Pt-Co alloy nanowire assemblies with tunable composition and enhanced electrocatalytic properties. *Angew. Chem., Int. Ed*. **2015**, *54*, 3797–3801.

[23] Li, C. L.; Imura, M.; Yamauchi, Y. Displacement plating of a mesoporous Pt skin onto Co nanochains in a low-concentration surfactant solution. *Chem.— Eur. J.* **2014**, *20*, 3277–3282.

[24] Gong, M. X.; Fu, G. T.; Chen, Y.; Tang, Y. W.; Lu, T. H. Autocatalysis and selective oxidative etching induced

synthesis of platinum-copper bimetallic alloy nanodendrites electrocatalysts. *ACS Appl. Mater. Interfaces* **2014**, *6*, 7301–7308.

[25] Stamenkovic, V. R.; Mun, B. S.; Arenz, M.; Mayrhofer, K. J. J.; Lucas, C. A.; Wang, G. F.; Ross, P. N.; Markovic, N. M. Trends in electrocatalysis on extended and nanoscale Pt-bimetallic alloy surfaces. *Nat. Mater*. **2007**, *6*, 241–247.

[26] Choi, D. S.; Robertson, A. W.; Warner, J. H.; Kim, S. O.; Kim, H. Low-temperature chemical vapor deposition synthesis of Pt-Co alloyed nanoparticles with enhanced oxygen reduction reaction catalysis. *Adv. Mater*. **2016**, *28*, 7115–7122.

[27] Bu, L. Z.; Guo, S. J.; Zhang, X.; Shen, X.; Su, D.; Lu, G.; Zhu, X.; Yao, J. L.; Guo, J.; Huang, X. Q. Surface engineering of hierarchical platinum-cobalt nanowires for efficient electrocatalysis. *Nat. Commun*. **2016**, *7*, 11850–11859.

[28] Ma, Z. Z.; Yu, H. C.; Wu, Z. Y.; Wu, Y.; Xiao, F. B. A highly sensitive amperometric glucose biosensor based on a nano-cube Cu_2O modified glassy carbon electrode. *Chin. J. Anal. Chem.* **2016**, *44*, 822–827.

[29] Zhang, Z. C.; Luo, Z. M.; Chen, B.; Wei, C.; Zhao, J.; Chen, J. Z.; Zhang, X.; Lai, Z. C.; Fan, Z. X.; Tan, C. L. et al. One-pot synthesis of highly anisotropic five-fold-twinned PtCu nanoframes used as a bifunctional electrocatalyst for oxygen reduction and methanol oxidation. *Adv. Mater*. **2016**, *28*, 8712–8717.

[30] Nosheen, F.; Zhang, Z. C.; Xiang, G. L.; Xu, B.; Yang, Y.; Saleem, F.; Xu, X. B.; Zhang, J. C.; Wang, X. Three-dimensional hierarchical Pt-Cu superstructures. *Nano Res*. **2015**, *8*, 832–838.

[31] Wang, W.; Lv, F.; Lei, B.; Wan, S.; Luo, M. C.; Guo, S. J. Tuning nanowires and nanotubes for efficient fuel-cell electrocatalysis. *Adv. Mater*. **2016**, *28*, 10117–10141.

[32] Su, Y. K.; Liu, H.; Feng, M.; Yan, Z. L.; Cheng, Z. H.; Tang, J. N.; Yang, H. T. Bimetallic Pt_3Co nanowires as electrocatalyst: The effects of thermal treatment on electrocatalytic oxidation of methanol. *Electrochim. Acta* **2015**, *161*, 124–128.

[33] Liang, H. W.; Liu, S.; Yu, S. H. Controlled synthesis of one-dimensional inorganic nanostructures using pre-existing one-dimensional nanostructures as templates. *Adv. Mater*. **2010**, *22*, 3925–3937.

[34] Zhang, Z. T.; Blom, D. A.; Gai, Z.; Thompson, J. R.; Shen, J.; Dai, S. High-yield solvothermal formation of magnetic CoPt alloy nanowires. *J. Am. Chem. Soc*. **2003**, *125*, 7528–7529.

[35] Liu, H. Q.; Adzic, R. R.; Wong, S. S. Multifunctional ultrathin Pd_xCu_{1-x} and $Pt\sim Pd_xCu_{1-x}$ one-dimensional nanowire motifs for various small molecule oxidation reactions. *ACS Appl. Mater. Interfaces* **2015**, *7*, 26145–26157.

[36] Hong, W.; Shang, C. S.; Wang, J.; Wang, E. K. Bimetallic PdPt nanowire networks with enhanced electrocatalytic activity for ethylene glycol and glycerol oxidation. *Energy Environ. Sci.* **2015**, *8*, 2910–2915.

[37] Zhang, J.; Cullen, D. A.; Forest, R. V.; Wittkopf, J. A.; Zhuang, Z. B.; Sheng, W. C.; Chen, J. G.; Yan, Y. S. Platinum−ruthenium nanotubes and platinum−ruthenium coated copper nanowires as efficient catalysts for electro-oxidation of methanol. *ACS Catal.* **2015**, *5*, 1468–1474.

[38] Zhao, X.; Zhang, J.; Wang, L. J.; Li, H. X.; Liu, Z. L.; Chen, W. Ultrathin PtPdCu nanowires fused porous architecture with 3D molecular accessibility: An active and durable platform for methanol oxidation. *ACS Appl. Mater. Interfaces* **2015**, *7*, 26333–26339.

[39] Xia, B. Y.; Wu, H. B.; Yan, Y.; Lou, X. W.; Wang, X. Ultrathin and ultralong single-crystal platinum nanowire assemblies with highly stable electrocatalytic activity. *J. Am. Chem. Soc.* **2013**, *135*, 9480–9485.

[40] Yin, A.-X.; Min, X.-Q.; Zhu, W.; Liu, W.-C.; Zhang, Y.-W.; Yan, C.-H. Pt-Cu and Pt-Pd-Cu concave nanocubes with high-index facets and superior electrocatalytic activity. *Chem.—Eur. J.* **2012**, *18*, 777–782.

[41] Liu, L. F.; Pippel, E.; Scholz, R.; Gösele, U. Nanoporous Pt-Co alloy nanowires: Fabrication, characterization, and electrocatalytic properties. *Nano Lett*. **2009**, *9*, 4352–4358.

[42] Lai, J. P.; Zhang, L.; Qi, W. J.; Zhao, J. M.; Xu, M.; Gao, W. Y.; Xu, G. B. Facile synthesis of porous PtM (M = Cu, Ni) nanowires and their application as efficient electrocatalysts for methanol electrooxidation. *ChemCatChem* **2014**, *6*, 2253–2257.

[43] Chang, F. F.; Yu, G.; Shan, S. Y.; Skeete, Z.; Wu, J. F.; Luo, J.; Ren, Y.; Petkov, V.; Zhong, C.-J. Platinum-nickel nanowire catalysts with composition-tunable alloying and faceting for the oxygen reduction reaction. *J. Mater. Chem. A* **2017**, *5*, 12557–12568.

[44] Zhou, Y. Z.; Yang, J.; Zhu, C. Z.; Du, D.; Cheng, X. N.; Yen, C. H.; Wai, C. M.; Lin, Y. H. Newly designed graphene cellular monolith functionalized with hollow Pt-M (M = Ni, Co) nanoparticles as the electrocatalyst for oxygen reduction reaction. *ACS Appl. Mater. Interfaces* **2016**, *8*, 25863–25874.

[45] Huang, H. J.; Fan, Y.; Wang, X. Low-defect multi-walled carbon nanotubes supported PtCo alloy nanoparticles with remarkable performance for electrooxidation of methanol. *Electrochim. Acta* **2012**, *80*, 118–125.

[46] Xue, Q. M.; Xu, S. B.; Yan, X.; Luo, B. J. Synthesis of worm-like PtCo nanotubes for methanol oxidation. *Electrochim. Commun.* **2013**, *30*, 71–74.

[47] Ahmadi, R.; Amini, M. K.; Bennett, J. C. Pt-Co alloy nanoparticles synthesized on sulfur-modified carbon nanotubes

as electrocatalysts for methanol electrooxidation reaction. *J. Catal.* **2012**, *292*, 81–89.

[48] Liao, Y.; Yu, G.; Zhang, Y.; Guo, T. T.; Chang, F. F.; Zhong, C. J. Composition-tunable PtCu alloy nanowires and electrocatalytic synergy for methanol oxidation reaction. *J. Phys. Chem. C* **2016**, *120*, 10476–10484.

[49] Chang, F. F.; Shan, S. Y.; Petkov, V.; Skeete, Z.; Lu, A. L.; Ravid, J.; Wu, J. F.; Luo, J.; Yu, G.; Ren, Y. et al. Composition tunability and (111)-dominant facets of ultrathin platinum-gold alloy nanowires toward enhanced electrocatalysis. *J. Am. Chem. Soc.* **2016**, *138*, *12166–12175.*

[50] Mourdikoudis, S.; Liz-Marzán, L. M. Oleylamine in nanoparticle synthesis. *Chem. Mater.* **2013**, *25*, 1465–1476.

[51] Alia, S. M.; Pylypenko, S.; Neyerlin, K. C.; Cullen, D. A.; Kocha, S. S.; Pivovar, B. S. Platinum-coated cobalt nanowires as oxygen reduction reaction electrocatalysts. *ACS Catal.* **2014**, *4*, 2680–2686.

[52] Yu, X. F.; Wang, D. S.; Peng, Q.; Li, Y. D. Pt-M (M = Cu, Co, Ni, Fe) nanocrystals: From small nanoparticles to wormlike nanowires by oriented attachment. *Chem.—Eur. J.* **2013**, *19*, 233–239.

[53] Wang, Q.; Li, Y. J.; Liu, B. C.; Xu, G. R.; Zhang, G.; Zhao, Q.; Zhang, J. A facile reflux procedure to increase active surface sites form highly active and durable supported palladium@platinum bimetallic nanodendrites. *J. Power Sources* **2015**, *297*, 59–67.

[54] Bertin, E.; Garbarino, S.; Ponrouch, A.; Guay, D. Synthesis and characterization of PtCo nanowires for the electro-oxidation of methanol. *J. Power Sources* **2012**, *206*, 20–28.

[55] Wang, Z. H.; Xie, W. F.; Zhang, F. F.; Xia, J. F.; Gong, S. D.; Xia, Y. Z. Facile synthesis of PtPdPt nanocatalysts for methanol oxidation in alkaline solution. *Electrochim. Acta* **2016**, *192*, 400–406.

[56] Xiao, M. L.; Li, S. T.; Zhu, J. B.; Li, K.; Liu, C. P.; Xing, W. Highly active PtAu nanowire networks for formic acid oxidation. *ChemPlusChem* **2014**, *79*, 1123–1128.

[57] Zeng, J. H.; Lee, J. Y. Effects of preparation conditions on performance of carbon-supported nanosize Pt-Co catalysts for methanol electro-oxidation under acidic conditions. *J. Power Sources* **2005**, *140*, 268–273.